16th World Conference on Earthquake Engineering, 16WCEE 2017
Santiago Chile, January 9th to 13th 2017
Paper N° 4023
Registration Code: S-V1464728356

WAVE PROPAGATION AND SOURCE MODELS FOR SYNTHETIC SEISMOGRAMS COMPATIBLE WITH STRONG MOTION APPLICATIONS

J. G. Anderson[(1)], R. J. Brune[(2)], J. N. Brune[(3)], G. P. Biasi[(4)]

[(1)] *Professor, University of Nevada, Reno, Nevada, U.S.A., jga@unr.edu*
[(2)] *Costa Mesa, California, U.S.A., richbrune@sbcglobal.net*
[(3)]*Professor Emeritis, University of Nevada, Reno, Nevada, U.S.A., brune@unr.edu*
[(4)]*Research Professor, University of Nevada, Reno, Nevada, U.S.A., glenn@unr.edu*

Abstract

The goal of this project is to generate realistic strong motion synthetic seismograms at distances of engineering significance, with emphasis on parameterizing the models with variables that are in standard use by seismologists. This approach is transferable to new regions, where strong motion data are sparse. Wave propagation is approximated with thin, flat, attenuating layers to approximate the local velocity gradient found by exploration seismology. The method produces seismograms with appropriately-polarized P-waves, S-waves, and surface waves. The attenuation model has high values of Q in the crustal waveguide (e.g. >5 km deep) to reproduce the distance dependence of the spectral amplitudes and of the spectral decay parameter (kappa), and low values of Q in shallow soil layers to reproduce the values of kappa extrapolated to zero distance (kappa-0).

The application we describe here simulates a M7.65 earthquake, approximating the southern end of where the 1857 rupture of the San Andreas fault passed Lovejoy Buttes with about 4 m of slip. Precarious rocks at Lovejoy Buttes mostly appear old enough that they survived the 1857 earthquake. Within the range of observed physical values for the input parameters, we can generate synthetic seismograms that topple very few of these rocks, and others that topple most of them. Thus calibrating with precarious rocks, the composite source model has the potential to explore source physics parameters as well as to provide realistic, constrained ground motions from future great earthquakes.

Keywords: Seismology, strong ground motion, synthetic time histories, ground motion models, kappa, precarious rocks

1. Introduction

Many engineering projects need time histories or strong motion seismograms in a terminology used among seismologists. If synthetic time histories can be made sufficiently realistic, they can be used as input to models of structures, in order to test a proposed project design. Many approaches are available to generate synthetics (e.g. [1] [2] [3] [4] [5] [6] [7]). The composite source model [8] has been developed with a priority on following the physics of the problem wherever practical. This paper will briefly describe the model, and then illustrate some of its features via a calibration exercise in southern California.

2. Model Description

The framework used to generate synthetic seismograms is the seismic representation theorem [9]. The displacement of the ground, $\mathbf{u}(\mathrm{x},t)$, at location **x** and time *t* is given by:

$$u_n(\vec{x},t) = \int_{-\infty}^{\infty} d\tau \iint_{\Sigma} \left[u_i\left(\vec{\xi},\tau\right)\right] c_{ijpq}\nu_j \frac{\partial G_{np}\left(\vec{x},t-\tau,\vec{\xi},0\right)}{\partial \xi_q} d\Sigma \qquad (1)$$

In Eq. 1, $u_n(\vec{x},t)$ gives the n^{th} component of the displacement of the ground at an arbitrary location $\vec{x}$ and at time *t*. The vector $\vec{\nu}$ is normal to the fault, and the positive direction of the normal defines the positive side of the fault for defining the slip discontinuity. The i^{th} component of the discontinuity in the slip across the fault is given by $\left[u_i\left(\vec{\xi},\tau\right)\right]$ where $\vec{\xi}$ represents a location on the fault surface, Σ, and τ is the time that this displacement occurs. The Green's function is given by $G_{np}\left(\vec{x},t-\tau,\vec{\xi},0\right)$. This gives the motion in the *n* direction at location $\vec{x}$ and time *t* caused by a an impulse point force acting in the *p* direction at location $\vec{\xi}$ and time τ. Finally, c_{ijpq} gives the elastic constants of the medium. We assume an isotropic medium, so $c_{ijpq} = \lambda_E \delta_{ij}\delta_{pq} + \mu\left(\delta_{ik}\delta_{jl} + \delta_{il}\delta_{jk}\right)$, where λ_E and μ are the Lame constants. By convention, in Eq. 1 summation takes place over repeated indices.

Although complicated in appearance, Eq. 1 simply represents the ground motion at the site as the sum (integral) of the contributions from each point on the fault surface. The duration of the rupture at each point is covered by the time convolution. Thus calculating ground motions requires specification of two contributions: the offset on the fault as a function of location and time, and a model for the wave propagation.

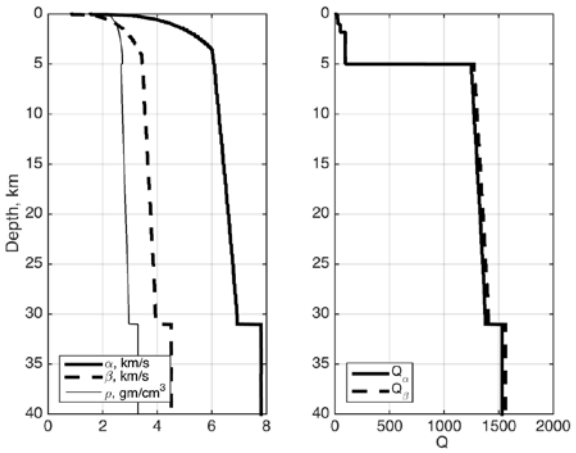

Fig. 1. Velocity and Q model used for the Mojave calculations. Realistic synthetics for these velocities require high Q in the deeper crustal waveguide and low Q in shallower layers to model greater heterogeneity and intrinsic attenuation mechanisms.

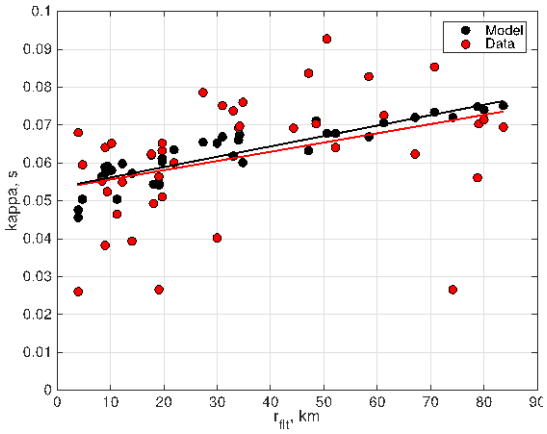

Fig. 2. Kappa consequences of Q model for a calibration with data from the Loma Prieta earthquake. The Loma Prieta velocity model is similar to the Mojave model shown in Fig. 1, except the Moho is at a depth of 25 km, instead of 31 km as in Fig. 1.

The Green's functions are calculated using the assumption of a flat-layered structure with frequency-independent Q. They are calculated using the numerical procedure described by Luco and Apsel [10], which is numerically stable for calculating response of a finely-layered velocity profile. Thus it is used to compute the Green's functions for the complete range of frequencies of interest, from 0 Hz to 25 Hz. Realistic velocity models for the crust often have velocity gradients as opposed to uniform layers. Because of the stability of the Luco and Apsel algorithm, the gradient can be approximated with thin layers (1 km or less is used here) all the way to the Moho. Globally, the Moho is typically ~40 km depth, but it is as shallow as ~25 km in parts of California. Fig. 1 shows the velocity model used to generate synthetic seismograms in this paper.

The Q model in Fig. 1 has been shown to be approximately consistent with the geometrical spreading deriving from the specific velocity model ([8] and unpublished results). Fig. 2 shows that the very low Q in the shallow layers, selected consistent with results of Assimaki et al. [11], and high Q in the crustal waveguide [8], results in the right dependence of kappa with distance. The distance dependence of spectral amplitudes is also tested (not shown) and found to be consistent with this model.

A feature of observed seismograms that is not generated by a flat-layered structure is the coda. First order properties of the coda have been characterized by the single-scatering model of Aki [12], and although there have been subsequent improvements to this model (e.g. [13] [14]), the present implementation of the CSM generates a coda using the single-scattering approach. The effect of this scattering is implemented as a convolution with the synthetic Green's function. Scatterers are not along the direct path from the source to the site, but convolution of the coda function with a Green's function for radial motion, for instance, will still be polarized in the radial direction. Thus a coda generated from all three components of the Green's function is added to each component, with the phase of the coda from one of the horizontal components scrambled using a Hilbert transform.

The source is a superposition of overlapping circular subevents. The magnitude of each subevent is chosen at random according to a Gutenberg-Richter relationship with b-value of 1.0. The number of subevents is chosen to match the seismic moment of the earthquake being synthesized. The subevents are distributed randomly, uniformly on the fault. A hypocenter is chosen at random as well, and then each subevent radiates a Brune pulse [15] at its rupture time. This time is found assuming a constant rupture velocity starting at the hypocenter. This source model is motivated by Frankel [16], as described by Zeng et al. [1].

The stress drop of the subevents, $\Delta\tau_S$, is a critical parameter. Higher values of $\Delta\tau_S$ have two effects: the number of subevents is decreased because the slip in each subevent is increased, and the radiation from each subevent is increased. In the complete seismograms that result, since the moment is fixed, the total low frequency radiation does not change with a change in subevent stress drop, but the energy radiated at high frequencies is increased. Thus higher values of $\Delta\tau_S$ are associated with higher apparent stress [17].

3. Calibration Exercise

3.1 Description

Fig. 3 shows a map of southern California, including the San Andreas fault and Lovejoy Buttes. The modeled part of the San Andreas fault is a relatively linear section bounding the Mojave Desert to the north, and the San Gabriel Mountains to the south. The geological structure of the Mojave Desert is relatively simple and spatially uniform, so the flat-layered structure in Fig. 1 is reasonable. Lovejoy Buttes are low granitic hills in the Mojave Desert. Brune [18] has found several somewhat precarious rock features in the Lovejoy Buttes that are believed to be very old (Fig. 4). The most recent major earthquake on this part of the San Andreas fault occured in 1857. The rock features found by Brune ([18]) would almost certainly have experienced the 1857 earthquake in their present geometry. We generated synthetic seismograms for locations of 15 rocks (Fig. 3), and determined if they would topple the rocks.

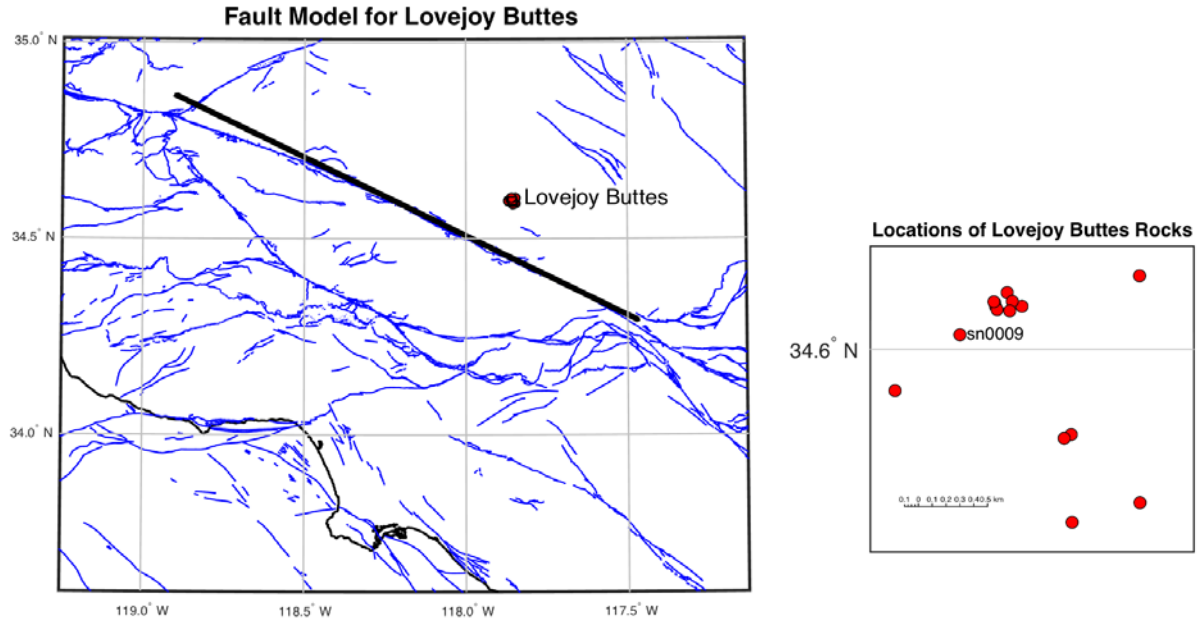

Fig. 3. Map of southern California, showing the coastline (black), major faults (blue), Lovejoy Buttes, and the model fault used to generate synthetic seismograms (heavy black). Location in ruptures runs from zero at the southeast end to 146 km at the northwest end. Lovejoy Buttes is nearest the fault at ~45 km. The small map at right shows relative locations of the rocks at Lovejoy Buttes. Rock 9, mentioned in the text, is highlighted.

In winter-early spring 2016, two of us (J. N. Brune and R. J. Brune) developed 3-dimensional models of the 15 rocks located in Fig. 3. The 3-D response of these rocks to any seismogram can thus be evaluated.

The composite source model (CSM) was used to generate synthetics for ruptures on the 146 km segment of the San Andreas fault highlighted in Fig. 3. The magnitude of the 1857 earthquake is estimated to be M_W7.9 [19], and the average slip on the Mojave Desert part modeled was about 4 m [20]. The approximate model for the southern end of the 1857 rupture was assigned M_W7.65, implying 4.2 m average slip. Shaking from the more northerly part of the 1857 rupture would be attenuated by the distance, so we believe that the M_W7.65 model gives a reasonable approximation to the shaking at Lovejoy Buttes that the CSM would produce from a full model of the 1857 event.

Fig. 4. Photos of three of the rocks located in Fig. 3 and used to test these simulations. The rock on the left (Rock 12 in Fig. 12) was toppled 39 times by the 20 bar source models, and all of the 60 bar source models (50 models). The center rock (Rock 2 in Fig. 12) was toppled by four of the 20 bar calculations, but by 43 of the 60 bar source models. The rock on the right side of the outcrop in the photo on the right (Fock 1 in Fig. 12), with the San Andreas fault at the front of the mountains in back, was toppled by ten of the 20 bar source models, and by 43 of the 60 bar source models.

3.2 Accelerogram properties

Figs. 5 – 8 show examples of four source functions, and associated synthetic seismograms, for Rock 9 (Fig. 3) of Lovejoy Buttes, located 15.3 km from the fault. The source realizations are chosen to illustrate toppling features that are discussed in the subsequent section. One realistic feature to notice in these seismograms are the permanent displacements at the station in the direction that is expected from the permanent offset at the fault. The velocity is dominated by strong, long-period pulses that vary depending on the rupture direction. On this scale, the envelope of the acceleration seems plausible, but it is difficult to see the details.

Before focusing on the Lovejoy Buttes calibration using precarious rocks, it is worthwhile to look at two characteristics of the CSM synthetics. First, an example of the polarization of the ground acceleration is shown in Fig. 9. Especially for strike-slip faulting, one expects that the wavefield will be dominated by SH-waves, so it should be possible to follow the progress of the rupture by changes in the polarization. Fig. 9 indeed shows this effect very clearly for a station 50 km north of the fault.

Another general feature of CSM synthetics is illustrated in Fig. 10. Here the acceleration is shown filtered with different frequency bands. For comparison, we show the strong motion recorded at the Sakarya record of the 1999 Kocaeli, Turkey earthquake (M_W7.4). Sakarya is about midway along the rupture, and 3.1 km from the fault [21]. Both accelerogram in Fig. 10 have pulses of energy that, in different frequency bands, arrive at different times. In the CSM synthetics, these are due to contributions of different subevent sizes at different random times.

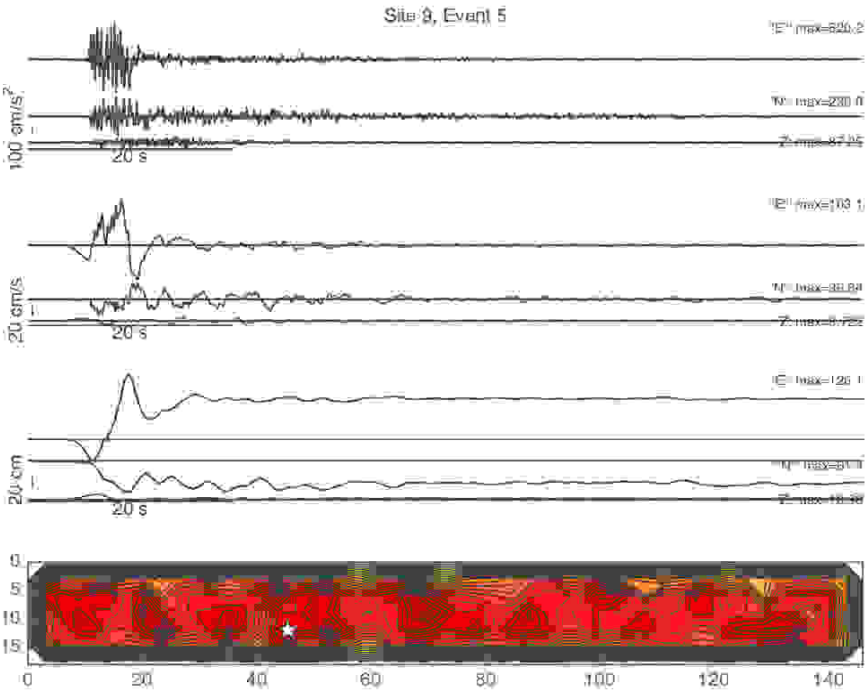

Fig. 5. Acceleration, velocity, and displacement seismograms generated for Lovejoy Rock #9, using $\Delta\tau_S$ =20 bars and Mw=7.65. The peak amplitude of each synthetic seismogram is shown on the right. The bottom frame shows a representation of source model #5 used to generate these seismograms. As noted in the caption for Fig. 3, zero distance in the length scale for the source representation is at the southeast end and Lovejoy Buttes project onto the fault at 45 km. Thus for this source realization, the hypocenter (star) is close to the point on the fault nearest to Lovejoy Buttes.

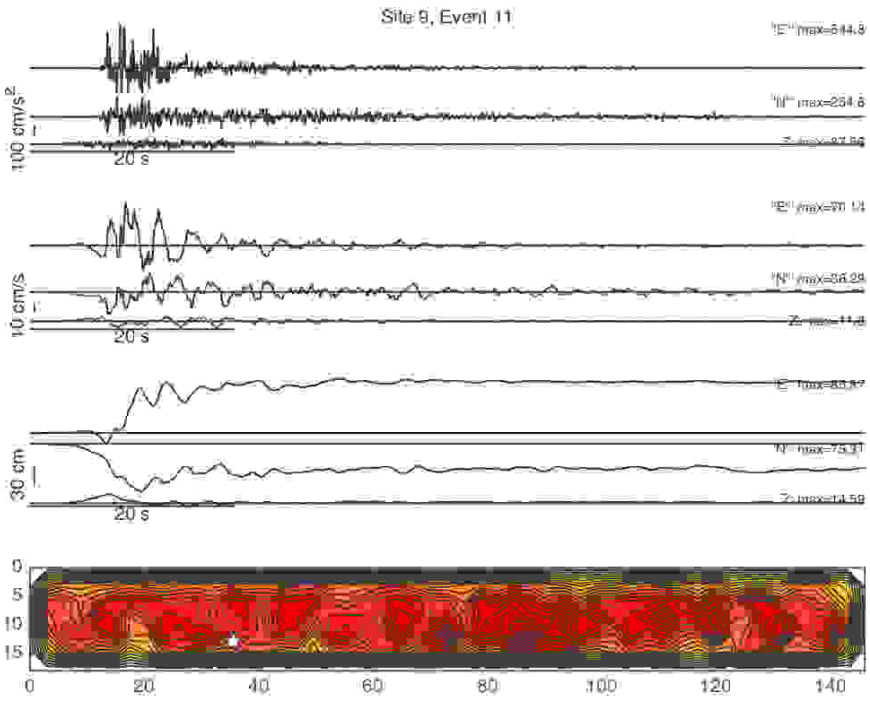

Fig. 6. Equivalent to Fig. 5 for source model #11. As for Source 5, the hypocenter is close to Lovejoy Buttes., but this source model caused only one of the rocks to topple.

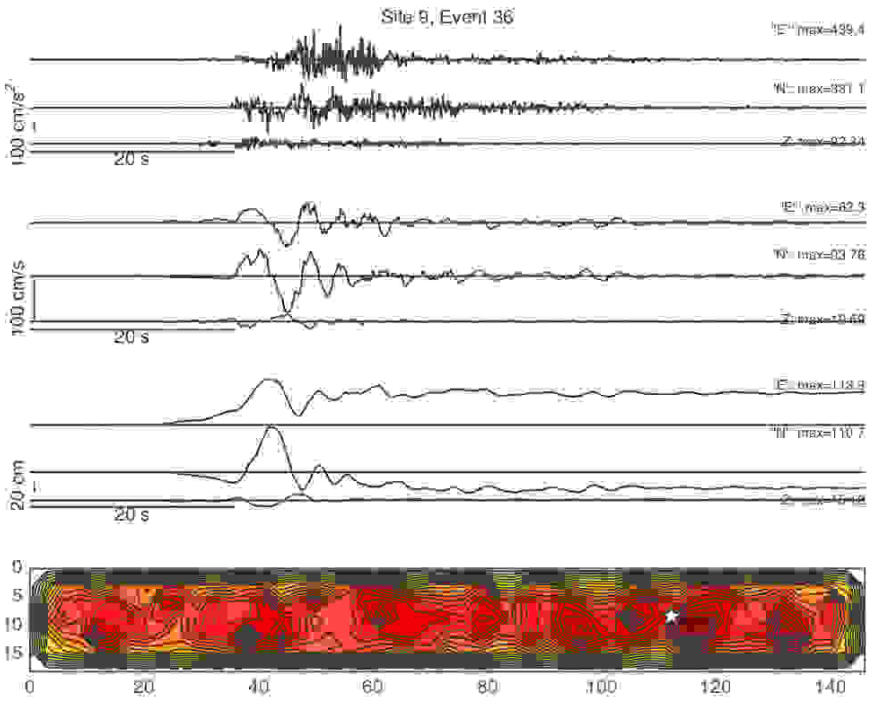

Fig. 7. Equivalent to Fig. 5 for source model #36. Since this hypocenter is far from Lovejoy Buttes directivity is expected to be strong. However, this source model would not cause any of the rocks at Lovejoy Buttes to topple.

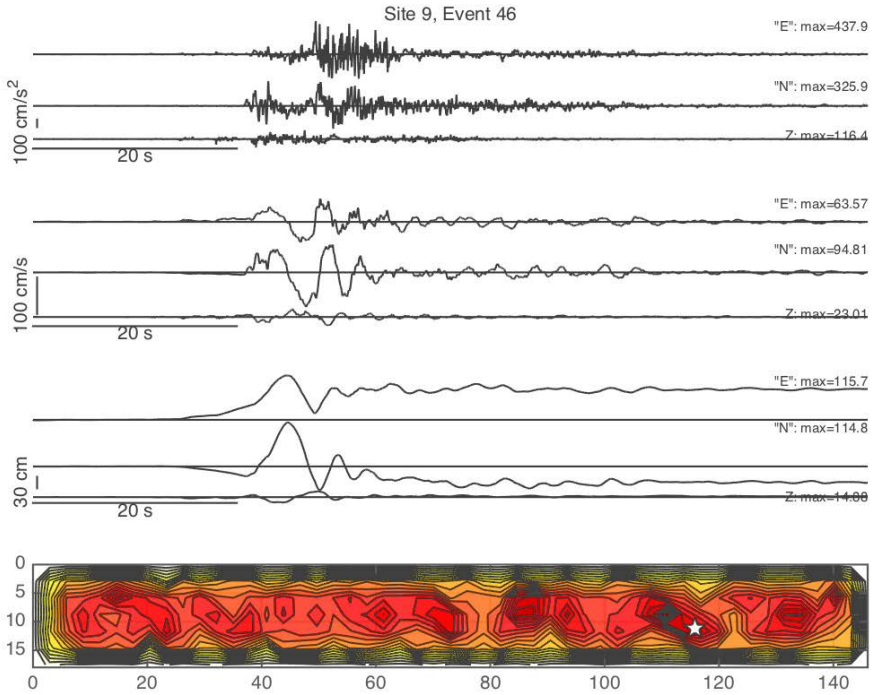

Fig. 8. Equivalent to Fig. 5 for source model #46. Note that the hypocenter is far from Lovejoy Buttes, close to the hypocenter in Fig. 7. This source model caused 5 of the rocks to topple.

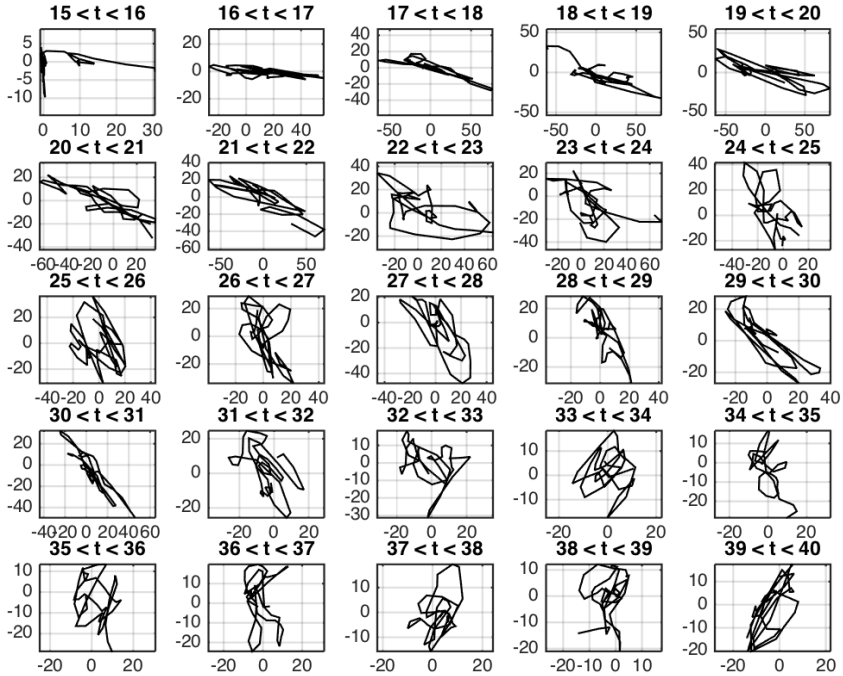

Fig. 9. Polarization of ground motions in different time windows at a station 50 km from the M_W7.65 model fault in Fig. 3. The station, not shown on the map, is located on a line perpendicular to the fault running through Lovejoy Buttes. At this station, the first S-wave from a hypocenter near Lovejoy Buttes arrives at t~15.7 s. The direct S-waves continue beyond the last time window shown here. Rupture is proceeding to the northwest, and the S-waves particle accelerations, dominated by SH, are rotating as they remain predominantly perpendicular to the backazimuth.

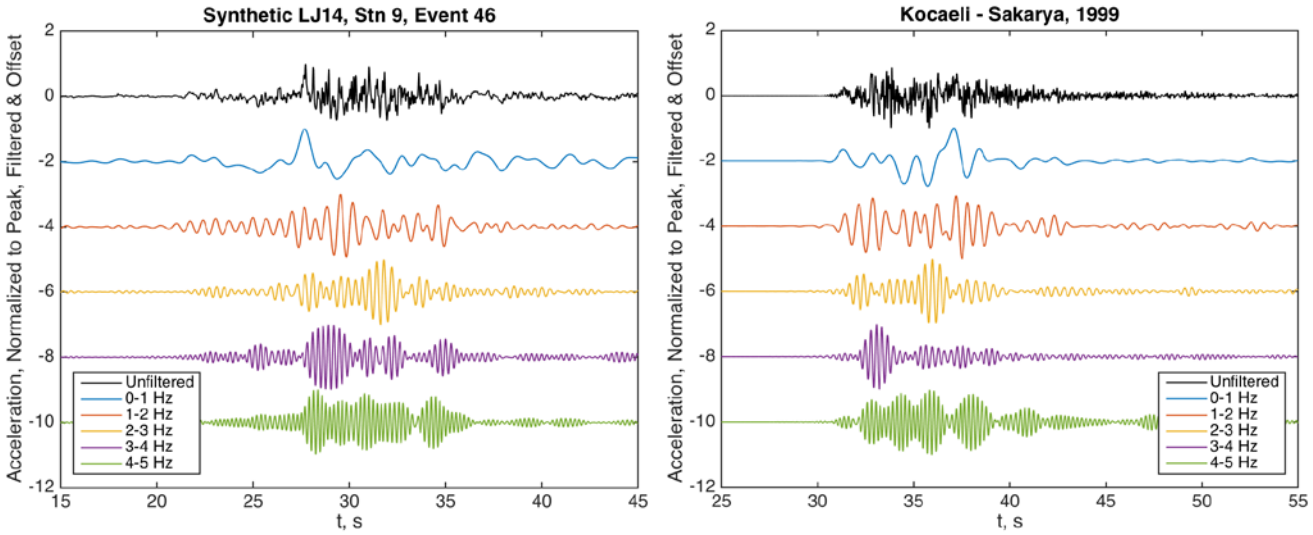

Fig. 10. Left: Synthetic accelerograms for rupture starting relatively far from Lovejoy Buttes and propagating past the station. The band pass filters are acaual 6-pole Butterworth filter, with corner frequencies indicated in the legend. All traces are normalized to the peak value, and filtered records are offset. Right: Acceleration from the Sakarya station, recorded in the 1999 Kocaeli, Turkey earthquake (Mw=7.4).

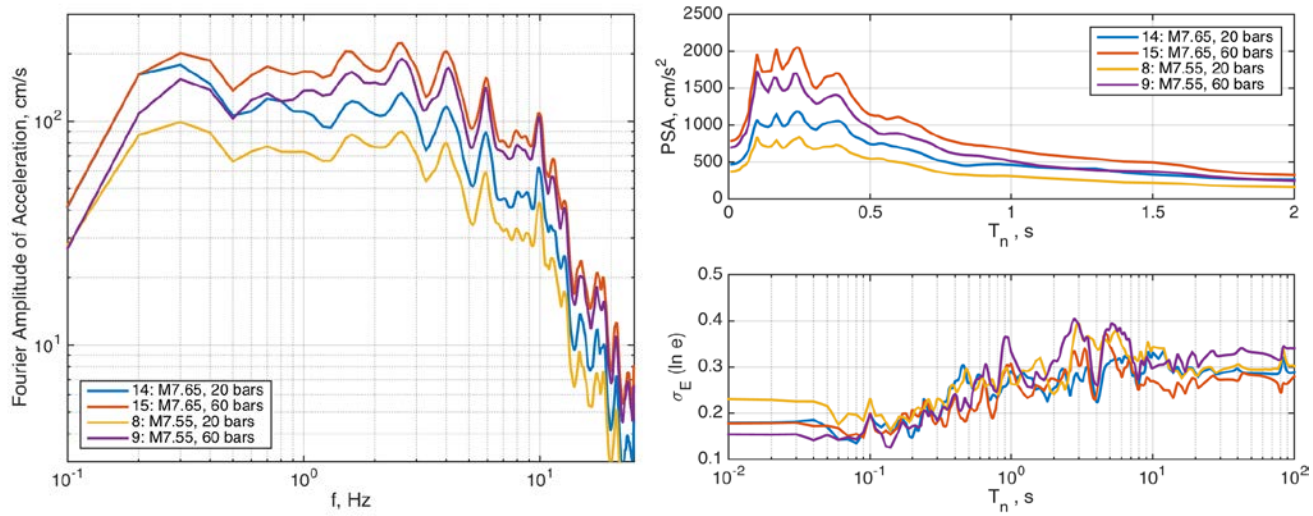

Fig. 11. Left: Average Fourier amplitude spectrum for Rock 9 (Fig. 3) for four source models, as discussed in the text. Right: Average pseudo-acceleration response spectra (PSA, 5% damping) corresponding to the same source models. The uncertainty due to the source variability, estimated from the 50 realizations, is shown for the full range of periods, while the spectra themselves are plotted on a linear scale that shows only the periods with the highest amplitudes.

3.3 Application to the Lovejoy Buttes rocks

The synthetics for Lovejoy Buttes were prepared for two different values of $\Delta\tau_S$, 20 bars and 60 bars, and for magnitudes 7.55 and 7.65. The average slips are 300 cm and 420 cm, respectively. The two magnitudes thus primarily illustrate the dependence on average slip. Fig. 11 shows the average Fourier amplitude spectra and PSA response spectra calculated for rock 9, for 50 realizations with each combination of source parameters. The average low frequencies converge to different values depending on magnitude or average slip. On the other hand, the high frequencies, while affected by magnitude, are strongly dependent on $\Delta\tau_S$.

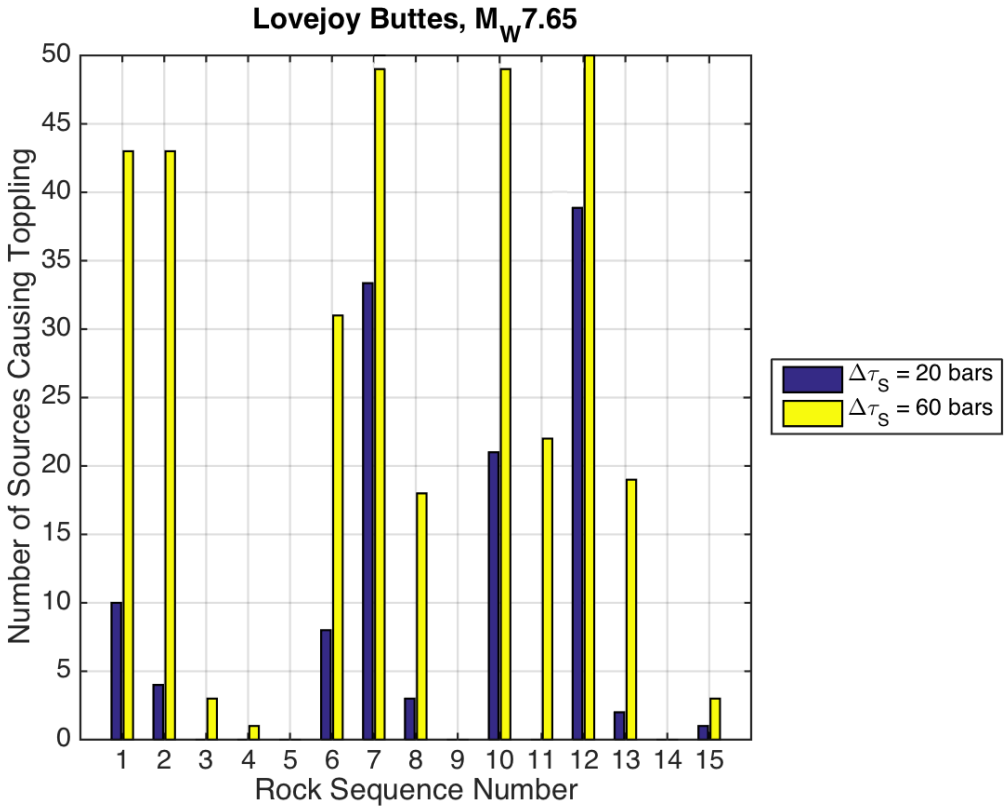

Fig. 12. Histogram of toppling counts for 50 realizations of synthetics for precarious rocks at Lovejoy Buttes, for two source models. Both models are on the approximation to the San Andreas fault shown in Fig. 3, and use Mw=7.65, implying that the average slip on the fault is 420 cm. They differ in subevent stress drop, as indicated in the legend.

Since the 1857 average slip is believed to be about 400 cm, Fig. 12 shows toppling statistics for the M_W7.65 model, for $\Delta\tau_S$ of 20 bars and 60 bars. Three of the rocks toppled in more than 10 of the source realizations with $\Delta\tau_S$ of 20 bars, while 9 of the 15 rocks are modeled to topple that frequently for $\Delta\tau_S$ of 60 bars. Thus by this test, $\Delta\tau_S$ of 20 bars would be preferred for generating synthetic seismograms for events of this magnitude. We note that for the M7.55 earthquake, only two rocks topple for more than one of the 50 source realizations with $\Delta\tau_S$ of 20 bars, while the results for 60 bars are in between the two cases shown on Fig. 12. These results are consistent with the relative amplitudes of the spectra in Fig. 11.

The events in Figs. 5-8 were chosen to illustrate effects of directivity and spatial variability of fault slip. Figures 5 and 6 select source realizations with minimal directivity at Lovejoy Buttes, since Lovejoy Buttes project onto the fault close to these hypocenters. Realization 5 (Fig. 5) causes 5 rocks to topple while realization 11 (Fig. 6) causes only 1 to topple. Realization 36 (Fig. 7) has rupture propagation towards Lovejoy Buttes, but no rocks are toppled, while the similar realization 46 (Fig. 8) causes 5 to topple. These results suggest that for precarious rocks at the distance of Lovejoy Buttes from the fault, in the composite source model the distribution of slip patches is more important than directivity.

Another interesting feature was recognized by considering what would happen to these rocks if they were rotated around a vertical axis and then exposed to the same ground motions. Interestingly, the number that would be toppled increased significantly. This suggests that the polarization of the synthetic seismograms is also being tested by this numerical exercise. A purely random polarization, not incorporating the physics built into the composite source model, would not show this effect. One feature of the particle motion is that the acceleration (high frequencies) is predominantly polarized in the fault-parallel direction, consistent with high frequencies dominated by SH waves radiated on the nearest section of the fault. The velocity and displacement (low frequencies) are more often polarized more in a fault-normal direction, consistent with the large fault-normal pulses expected from directivity in the forward propagation direction from the fault.

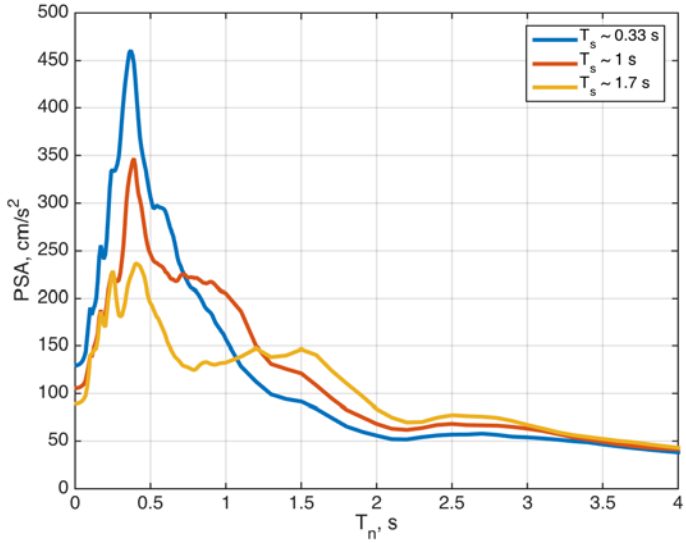

Fig. 13. Sensitivity of synthetic seismograms to the upper 100 m of the velocity model. These three spectra (averaged over 50 realizations each) have Vs30=250 m/s, but shallow models are created to have different site periods, T_S, as indicated in the legend. Below 100 m, the velocity model is identical to the model in Fig. 1, starting with a 30 meter thick layer having Vs=863 m/s. The peak at short periods comes partly from deeper structure (Fig. 2) and the earthquake source (Fig. 3), but is enhanced by the site model with 0.33s resonant period.

4. Discussion and Conclusions

This paper has briefly summarized some of the physical phenomena that affect strong ground motion and are built into the composite source model. The reasonable range of parameters that characterize these phenomena is known. The application discussed in this paper is to combine these phenomena to generate synthetic seismograms intended to approximate the great 1857 earthquake on the San Andreas fault. Some of the synthetics generated in this way would destroy precarious rocks that survived the 1857 earthquake, while others that are intentionally less energetic would not. We consider it a success that the synthetics span this threshold, since the observed rocks, being the most precarious that have been discovered in the study area, are themselves on the threshold of survival. Thus the results confirm the premises on which the composite source model is built and present the opportunity to calibrate the model for a magnitude and distance range lacking in instrumental observations. The figures presented here are not a complete exploration of the physical parameter space encompassed in the composite source model synthetics, but they do demonstrate that such an exploration will lead to meaningful, useful results.

The wave propagation model that is used to generate the composite source model synthetics is based on the physics of elastic waves in flat-layered media. One important point is that the model can handle thin layers even though the synthetics can be generated at distances of tens to a couple hundred kilometers or more. For example, Fig. 13 shows response spectra for seismograms generated 50 km from the fault using three different models of the upper 100 m, with differing site resonant periods. The three response spectra are quite different. This illustrates the potential to merge site response with wave propagation from the source for improved synthetic seismograms. However the challenge of incorporating a general site response remains to be solved.

A critical issue is acceptance criteria: how can we decide if a seismogram (either synthetic or scaled) is "good enough" for engineering applications. For instance the SCEC Broadband Project has up to this point focused heavily on the ability to recover response spectra. This is of course reasonable for some engineering applications. However seismograms can be very rich in other properties that derive from wave propagation or source characteristics. If it is known which and how many of those need to be preserved in synthetics for various types of engineering applications, synthetics that incorporate those phenomena can probably be developed.

5. Acknowldegements

This research was supported by the Southern California Earthquake Center (Contribution No. 6266). SCEC is funded by NSF Cooperative Agreement EAR-1033462 & USGS Cooperative Agreement G12AC20038.

5. References

[1] Zeng, Y., Anderson, J. G. & Yu, G. A composite source model for computing realistic synthetic strong ground motions. *Geophysical Research Letters* **21**, 725–728 (1994).
[2] Kamae, K., Irikura, K. & Pitarka, A. A technique for simulating strong ground motion using hybrid Green's function. *Bulletin of the Seismological Society of America* **88**, 357–367 (1998).
[3] Boore, D. Simulation of ground motion using the stochastic method. *Pure and Applied Geophysics* **160**, 635–676 (2003). Scientific Meeting on Seismic Motion, Litospheric Structures, Earthquake and Volcanic Sources, UNIV SO CALIF, LOS ANGELES, CALIFORNIA, MAR 16-18, 2000.
[4] Graves, R. & Pitarka, A. Refinements to the Graves and Pitarka (2010) broadband ground-motion simulation method. *Seismological Research Letters* **86**, 75–80 (2015).
[5] Olsen, K. & Takedatsu, R. The SDSU broadband ground-motion generation module bbtoolbox version 1.5. *Seismological Research Letters* **86**, 81–88 (2015).
[6] Crempien, J. G. F. & Archuleta, R. J. UCSB method for simulation of broadband ground motion from kinematic earthquake sources. *Seismological Research Letters* **86**, 61–67 (2015).
[7] Atkinson, G. M. & Assatourians, K. Implementation and validation of exsim (a stochastic finite-fault ground-motion simulation algorithm) on the scec broadband platform. *Seismological Research Letters* **86**, 48–60 (2015).
[8] Anderson, J. G. The composite source model for broadband simulations of strong ground motions. *Seismological Research Letters* **86**, 68–74 (2015).
[9] Aki, K. & Richards, P. *Quantitative seismology* (Univ Science Books, 2002).
[10] Luco, J. E. & Apsel, R. J. On the green's functions for a layered half-space. part i. *Bulletin of the Seismological Society of America* **73**, 909–929 (1983).
[11] Assimaki, D., Li, W., Steidl, J. H. & Tsuda, K. Site amplification and attenuation via downhole array seismogram inversion: a comparative study of the 2003 Miyagi-Oki aftershock sequence. *Bulletin of the Seismological Society of America* **98**, 301–330 (2008).
[12] Aki, K. & Chouet, B. Origin of coda waves: source, attenuation, and scattering effects. *Journal of Geophysical Research* **80**, 3322–3342 (1975).
[13] Zeng, Y. Compact solutions for multiple scattered wave energy in the time domain. *Bulletin of the Seismological Society of America* **81**, 1022–1029 (1991).
[14] Calvert, M. & Margerin, L. Lapse-time dependence of coda q: anisotropic multiple-scattering models and application to the pyrenees. *Bulletin of the Seismological Society of America* **103**, 1993–2010 (2013).
[15] Brune, J. N. Tectonic stress and spectra of seismic shear waves from earthquakes. *Journal of Geophysical Research* **75**, 4997–& (1970).
[16] Frankel, A. High-frequency spectral falloff of earthquakes, fractal dimension of complex rupture, b value, and the scaling of strength of faults. *Journal of Geophysical Research* **96**, 6291–6302 (1991).
[17] Wyss, M. & Molnar, P. Efficiency, stress drop, apparent stress, effective stress, and frictional stress of Denver, Colorado, earthquakes. *Journal of Geophysical Research* **77**, 1433–& (1972).
[18] Brune, J. Precariously balanced rocks and ground-motion maps for southern California. *Bulletin of the Seismological Society of America* **86**, 43–54 (1996).
[19] Zielke, O., Arrowsmith, J. R., Ludwig, L. G. & Alciz, S. O. Slip in the 1857 and earlier large earthquakes along the carrizo plain, san andreas fault. *Science* **327**, 1119–1122 (2010).
[20] Madden, C. *et al.* Appendix R—compilation of slip-in-the-last-event data and analysis of last event, repeated slip, and average displacement for recent and prehistoric ruptures. Open File Report 2013-1165, U. S. Geological Survey, Reston, Virginia (2013).
[21] Anderson, J. G. *et al.* Implications for seismic hazard analysis. *Earthquake Spectra* **16**, 113–137 (2000).